

Frustrated magnetism and quantum transitions of nematic phases in FeSe

Wen-Jun Hu¹, Hsin-Hua Lai¹, Shou-Shu Gong²,
Rong Yu^{3,4}, Andriy H. Nevidomskyy¹, and Qimiao Si¹

¹*Department of Physics and Astronomy & Rice Center for Quantum Materials,
Rice University, Houston, Texas 77005, USA*

²*National High Magnetic Field Laboratory,
Florida State University, Tallahassee, Florida 32310, USA*

³*Department of Physics, Renmin University of China, Beijing, 100872, China and*

⁴*Department of Physics and Astronomy,
Shanghai Jiao Tong University, Shanghai 200240,
China and Collaborative Innovation Center of Advanced Microstructures, Nanjing 210093, China*

Abstract

Unconventional superconductivity often emerges near antiferromagnetic order. This paradigm applies to many iron-based superconductors, but the iron chalcogenide FeSe represents a major puzzle. Its normal state has a nematic order (spontaneously broken lattice rotational symmetry) which, in contrast to the iron pnictides, is not accompanied by an antiferromagnetic order. In one proposal, such properties of FeSe originate from the orbital degrees of freedom associated with the Fe's 3d electrons. In a competing proposition, spin physics is central to FeSe but magnetic frustration has replaced antiferromagnetism with a more exotic spin state. Here, we show that a frustrated spin-1 bilinear-biquadratic model on the square lattice displays quantum transitions between non-magnetic and antiferromagnetic phases, each of which is also nematic. Our large-scale density matrix renormalization group calculations show that tuning the ratio of competing interactions in the model induces a transition from a $(\pi, 0)$ antiferroquadrupolar order to a $(\pi, 0)$ antiferromagnetic state, either directly or through a $(\pi/2, \pi)$ antiferromagnetic order. Our findings explain the recent dramatic experimental observations of an orthorhombic antiferromagnetic order in the pressurized FeSe, and suggest that superconductivity in a wide range of iron-based materials has a common origin.

Understanding the iron-based superconductors (FeSCs) has been a subject of extensive research in recent years.¹⁻³ The initial interest came with the discovery of superconductivity in the iron pnictides. More recently, iron chalcogenides have added considerable material varieties to this intriguing field and held the record of superconducting transition temperature (T_c) in FeSCs. These include the potassium iron selenides and other intercalated FeSe systems,⁴ as well as the single-layer FeSe built on substrates.^{5,6} Because all these involve FeSe as a building block, it is important to understand the physics of the bulk FeSe.^{7,8} Indeed, there is an intensive current interest in this system, which possesses the simplest structure among the FeSCs. It displays a tetragonal-to-orthorhombic structural transition, with $T_s \approx 90$ K at ambient pressure, but no magnetic long-range order.⁹⁻¹⁶ This phenomenology differs from the standard case of the iron pnictides, where the structural phase transition is accompanied by a $(\pi, 0)$ antiferromagnetic (AFM) order.^{2,3,17}

Several studies have advanced the proposals which attribute this unusual behavior of FeSe to the frustrated magnetism among the interaction-induced local moments.¹⁸⁻²⁰ A non-magnetic, antiferroquadrupolar (AFQ) state with wave vector $(\pi, 0)$ appears as a result of frustrated magnetism and has the properties of the bulk FeSe.¹⁸ An added appeal of the theoretical picture is that the predicted spin excitations, both for low energies near the wavevector $(\pi, 0)$ and over a wide ranges of energy and wave vector, have been verified by recent experiments.²¹⁻²⁴ Meanwhile, parallel proposals^{11,12,25} invoke the ordering of the electrons residing on Fe's $3d_{xz}$ and $3d_{yz}$ orbitals, which are degenerate in the C_4 -symmetric (tetragonal) phase above T_s . This idea is also appealing, because the splitting between the two $3d$ orbitals have been observed in the ARPES experiments in FeSe.¹³⁻¹⁵ Determining which of these competing ideas captures the essential physics is important to understanding the central microscopic ingredients for the normal state of the FeSCs as well as elucidating the degree to which the mechanism for superconductivity is universal across the varieties of the FeSCs.

In this paper, we address the issue by exploring the quantum phase transitions out of the nematic phase of FeSe. On general grounds, models with differing microscopic degrees of freedom will have different types of phases in their phase diagrams and, thus, different kinds of quantum phase transitions. Further motivation comes from recent experiments. The NMR²⁶ and X-ray scattering²⁷ measurements in pressurized FeSe have demonstrated that, lowering temperature induces a tetragonal to orthorhombic (OR) transition which accompanies a magnetic transition.

Our starting point is a spin-1 bilinear-biquadratic model on the square lattice, which builds on

theoretical studies of FeSe and other FeSCs.^{18,19,28–31} The model is defined as

$$H = \sum_{i,j} [J_{ij} \mathbf{S}_i \cdot \mathbf{S}_j + K_{ij} (\mathbf{S}_i \cdot \mathbf{S}_j)^2], \quad (1)$$

where \mathbf{S}_i is a spin-1 operator at site i , J_{ij} and K_{ij} are respectively the bilinear and biquadratic couplings between the spins at sites i and j , with i, j belonging to distinct bonds. Besides the usual spin operator, we also need to consider the quadrupolar operator \mathbf{Q}_i , which has five components: $Q_i^{x^2-y^2} = (S_i^x)^2 - (S_i^y)^2$, $Q_i^{3z^2-r^2} = [2(S_i^z)^2 - (S_i^x)^2 - (S_i^y)^2]/\sqrt{3}$, $Q_i^{xy} = S_i^x S_i^y + S_i^y S_i^x$, $Q_i^{yz} = S_i^y S_i^z + S_i^z S_i^y$, and $Q_i^{zx} = S_i^z S_i^x + S_i^x S_i^z$. The biquadratic term in Eq. (1) can be re-expressed as $(\mathbf{S}_i \cdot \mathbf{S}_j)^2 = (\mathbf{Q}_i \cdot \mathbf{Q}_j)/2 - (\mathbf{S}_i \cdot \mathbf{S}_j)/2 + (\mathbf{S}_i^2 \mathbf{S}_j^2)/3$. Interactions beyond the nearest-neighbor ones have been recognized as important to the phase diagram. For a minimum model without loss of generality, we consider $J_1 = 1$ as the energy unit, $J_3 = 0$, and $-K_1 = K_2 = -K_3 = K > 0$. We will refer to the present model as J_1 - J_2 - K model.

To explore the possible quantum phases of the model Eq. (1), we start from an analysis based on a site-factorized wave-function.^{18,30–32} The obtained phase diagram is illustrated in the J_2 - K plane in Fig. 1, which contains four stable phases: $\mathbf{q} = (\pi, 0)$ collinear AFM (CAFM) phase, $\mathbf{q} = (\pi/2, \pi)$ AFM* phase, $\mathbf{q} = (\pi, \pi)$ Néel AFM phase, and $\mathbf{q} = (\pi, 0)$ AFQ phase. The right panels of Fig. 1 illustrate the schematic configuration of each phase. The CAFM and Néel AFM have the conventional uniaxial and staggered spin patterns, respectively. The $(\pi, 0)$ AFQ is characterized by the mutually orthogonal nearest-neighbor directors (See Methods). The $(\pi/2, \pi)$ AFM* is an entirely new phase, in which the spin direction along the x -axis rotates with commensurate period of four sites while its period along the y -axis is still two sites reflecting the wave vector $(\pi/2, \pi)$. This AFM* state is nematic since it spontaneously breaks the C_4 symmetry, by choosing between two degenerate wave vectors $\mathbf{q} = (\pi/2, \pi)$ or $(\pi, \pi/2)$. For an illustration, the spin configuration of the $(\pi/2, \pi)$ AFM* state along the x -axis may take the 4-site periodic pattern as $\{|S^z = 1\rangle, |S^x = 1\rangle, |S^z = -1\rangle, |S^x = -1\rangle\}$, while the spin orientation still takes the conventional staggered pattern along the y -axis. Importantly, in the $(\pi/2, \pi)$ AFM* phase, the $\mathbf{q} = (\pi, 0)$ quadrupolar order parameter is nonzero as well, which is responsible for its stability.

Our analysis so far has been semi-classical. In order to explore the role of quantum fluctuations and analyze the model in an unbiased way, we have carried out large-scale density-matrix renormalization group (DMRG) calculations.³³ We consider the evolutions of the zero-temperature phases as a function of the biquadratic K coupling for fixed $J_2 = 1.5$ and 0.8 , respectively. Due to cylindrical geometry, the CAFM automatically selects the configuration with $\mathbf{q} = (0, \pi)$, whereas

the $(\pi/2, \pi)/(\pi, \pi/2)$ AFM* selects $\mathbf{q} = (\pi/2, \pi)$, and the AFQ phase selects $\mathbf{q} = (\pi, 0)$. In order to identify these phases, we have calculated the static spin and quadrupolar structure factors defined as

$$m_S^2(\mathbf{q}) = \frac{1}{L^4} \sum_{i,j} \mathbf{S}_i \cdot \mathbf{S}_j e^{i\mathbf{q} \cdot (\mathbf{r}_i - \mathbf{r}_j)}, \quad (2)$$

$$m_Q^2(\mathbf{q}) = \frac{1}{L^4} \sum_{i,j} \mathbf{Q}_i \cdot \mathbf{Q}_j e^{i\mathbf{q} \cdot (\mathbf{r}_i - \mathbf{r}_j)}, \quad (3)$$

where i, j are only partially summed over the $L \times L$ sites in the middle of cylinder in order to reduce finite-size effects.³⁴

For $J_2 = 1.5$ we identify a direct transition from CAFM to $(\pi, 0)$ AFQ at $K_c \simeq 0.65$. The evolutions of spin and quadrupolar structure factors shown in Fig. 2(a) simultaneously change dramatically at $K_c \simeq 0.65$, where the CAFM peak at $(0, \pi)$ melts and the AFQ peak at $(\pi, 0)$ develops rapidly. The finite-size scaling analysis of m_S^2 and m_Q^2 in Figs. 2(b)-(c) identifies the nonzero order in the thermodynamic limit for each phase.

For $J_2 = 0.8$, the system is CAFM at $K \lesssim 0.25$ and $(\pi, 0)$ AFQ at $K > 0.65$. In between, a new peak of spin structure factor develops at $\mathbf{q} = (\pi/2, \pi)$ as shown in Fig. 3(a), which characterizes the $(\pi/2, \pi)$ AFM* order. Our site-factorized wave-function analysis of the $(\pi/2, \pi)$ AFM* suggests the coexistence of the $(\pi/2, \pi)$ magnetic and $(\pi, 0)$ quadrupolar orders. In Figs. 3(b)-(c), the finite-size scalings of m_S^2 and m_Q^2 clearly demonstrate the nonzero values of both orders at $K \sim 0.6$. This signature is less clear for smaller K , but we expect that both orders already coexist there. We note that, for the 6×6 cluster, $\mathbf{q} = (\pi/2, \pi)$ is not one of the allowed wave vectors, and it may seem inappropriate to scale the m_S^2 data in this phase. However, the overall trend of m_S^2 is consistent with a nonzero $(\pi/2, \pi)$ magnetic order.

To characterize the nematicity in different phases, we introduce two nematic order parameters σ_1 and σ_Q defined as

$$\sigma_1 = \frac{1}{N_s} \sum_i [\langle \mathbf{S}_i \cdot \mathbf{S}_{i+\hat{x}} \rangle - \langle \mathbf{S}_i \cdot \mathbf{S}_{i+\hat{y}} \rangle], \quad (4)$$

$$\sigma_Q = \frac{1}{N_s} \sum_i [\langle \mathbf{Q}_i \cdot \mathbf{Q}_{i+\hat{x}} \rangle - \langle \mathbf{Q}_i \cdot \mathbf{Q}_{i+\hat{y}} \rangle], \quad (5)$$

where \hat{x} and \hat{y} denote the unit length along the x and y directions, respectively, and N_s is the number of lattice sites. The absolute value of the nematic order parameters as a function of K at $J_2 = 1.5$ and 0.8 are respectively presented in Figs. 4(a),(b). We find that σ_1 dominates over σ_Q inside the CAFM phase ($K \lesssim 0.65$ (0.25) for $J_2 = 1.5$ (0.8)), and σ_Q becomes dominant over σ_1

inside the $(\pi, 0)$ AFQ phase ($K \gtrsim 0.65$ for both J_2), showing the different primary origin of the nematicity. We also notice that the crossing of the two nematic order parameters occurs *exactly* at the location where the quadrupolar order at $\mathbf{q} = (\pi, 0)$ develops. For $J_2 = 1.5$, the crossing is at the boundary between CAFM and $(\pi, 0)$ AFQ; for $J_2 = 0.8$, it occurs at the boundary between CAFM and $(\pi/2, \pi)$ AFM*.

We now discuss the implications of our results for FeSe. Our work leads to two scenarios based on the presented phase diagram in Fig. 1(a). For clarity, we show a schematic phase diagram of the nematic phases in the inset of Fig. 4(c). Pressuring FeSe amounts to taking a cut in this phase diagram: we propose two such cuts as candidates for the parameter tuning, which are also illustrated in the inset of Fig. 4(c). The resulting phase diagram is illustrated in the main panel of Fig. 4(c), with the system undergoing either a direct transition between $(\pi, 0)$ AFQ and CAFM, or a transition between them through an intermediate $(\pi/2, \pi)$ AFM* regime with coexistence of magnetic and quadrupolar orders. This phase diagram is strikingly similar to that inferred from the recent experiments. While the presence of AFM order at pressures on the order of 2 GPa had been indicated before,³⁵ recent NMR measurements²⁶ have provided strong evidence that the order breaks the C_4 symmetry and has a $(\pi, 0)$ wave vector. The X-ray scattering experiments²⁷ have also provided evidence that a C_4 symmetry breaking accompanies the magnetic ordering. There are indications in the existing experiments for two stages of phase transitions under pressure,^{35–38} with the onset of AFM order around $p_1 \approx 0.8$ GPa and a change of the magnetic structure around $p_2 \approx 1.2$ GPa.³⁵ Further NMR and neutron-scattering measurements in the intermediate pressure range, $0.8 \text{ GPa} \lesssim P \lesssim 1.7 \text{ GPa}$ are especially called for to clarify this issue and ascertain which of the two proposed sequences applies.

The $(\pi, 0)$ AFQ order *per se* does not efficiently couple with the coherent conduction electrons near the Fermi surface. Still, the nematic order parameters, σ_1 and σ_Q defined in Eqs.(4) and (5) will linearly mix with the occupancy difference in the $3d_{xz}$ and $3d_{yz}$ orbitals, thereby generating a change in the electronic structure as has been extensively observed by ARPES experiments.^{13–15} By contrast, the $(\pi, 0)$ CAFM order will have a strong direct coupling with the conduction electrons, in addition to the coupling through σ_1 and σ_Q . This will induce additional changes to the Fermi surface. Thus, our proposed quantum phase transitions will be manifested in the changes to the geometry of Fermi surfaces. This is consistent with the dramatic change of the Fermi surface recently reported in the Shubnikov-de Haas (SdH) oscillation measurements.³⁹

The consistency of the quantum phase transitions we have identified in the frustrated bilinear-

biquadratic model with the experimental observations provides strong evidence that a similar type of spin physics is important for the superconductivity of both iron chalcogenides and iron pnictides. This is not to say that the orbital degrees of freedom are decoupled. As discussed above, the nematic order of the spin quadrupolar or dipolar orders will be coupled to the orbital order. Nonetheless, the interactions among the spin degrees of freedom as described in Eqs.(4) and (5) will give rise to superconducting pairing in FeSe – and, by extension, other iron chalcogenides – in a similar way as they do in the iron pnictides. Thus, our results not only yield the understanding of the striking recent experiments in FeSe, but also provide the evidence for a common origin of superconductivity across the extensive material classes of iron-based superconductors. More generally, our findings connect superconductivity of the highest T_c iron-based families with that arising near an antiferromagnetic order in a broad array of strongly correlated electron systems, including the cuprates and heavy fermion metals.

Methods

Site-factorized wave-function analysis We choose the time-reversal invariant basis of the $SU(3)$ fundamental representation: $|x\rangle = \frac{i|1\rangle - i|\bar{1}\rangle}{\sqrt{2}}$, $|y\rangle = \frac{|1\rangle + |\bar{1}\rangle}{\sqrt{2}}$, $|z\rangle = -i|0\rangle$, where we abbreviate $|S^z = \pm 1\rangle \equiv |\pm 1\rangle$ ($|S^z = 0\rangle \equiv |0\rangle$) and $|\bar{1}\rangle \equiv |-1\rangle$. Within this basis, the site-factorized wave-functions at each site i is expressed as a complex vector, $\mathbf{d}_i = (d_i^x \ d_i^y \ d_i^z)$, with the constraint $\mathbf{d}_i \cdot \bar{\mathbf{d}}_i = 1$ and the requirement $\mathbf{d}_i^2 = \bar{\mathbf{d}}_i^2$. In a quadrupolar state, \mathbf{d} will take a purely real or imaginary value, but not both, and the associated director is parallel to the director vector \mathbf{d} . This is to be contrasted with a magnetic order, for which a nonzero dipolar magnetic moment arises from a vector \mathbf{d} that contains both real and imaginary components. The energy per site of each phase can be obtained analytically, which leads to the determination of the phase boundaries. In the notation of [Phase 1] / [Phase 2], these are as follows: (1) [Néel AFM] / $[(\pi, 0)$ AFQ]: $K + 2J_2 - 2 = 0$; (2) [Néel AFM] / $[(\pi/2, \pi)$ AFM*]: $K - 8J_2 + 4 = 0$; (3) $[(\pi/2, \pi)$ AFM*] / [CAFM]: $11K - 8J_2 + 4 = 0$; (4) $[(\pi/2, \pi)$ AFM*] / $[(\pi, 0)$ AFQ]: $5K - 4 = 0$; (5) [CAFM] / $[(\pi, 0)$ AFQ]: $2K - J_2 = 0$.

DMRG calculations We perform the density matrix renormalization group simulations with spin rotational $SU(2)$ symmetry on the $L \times 2L$ cylinder systems with $L = 4, 6, 8$ in the y direction. The cylinder geometry has open boundary conditions along the x direction and periodic boundary conditions along the y direction. We keep up to 4000 $SU(2)$ DMRG states for the $L = 8$ cluster. In the Néel and CAFM phases, the truncation error is around 10^{-6} ; in the $(\pi/2, \pi)$ AFM* and

$(\pi, 0)$ AFQ phases, the truncation error is around 10^{-5} . The small truncation errors ensure us to obtain accurate DMRG results.

-
- ¹ Kamihara, Y., Watanabe, T., Hirano, M. & Hosono, H. Iron-Based Layered Superconductor $\text{La}[\text{O}_{1-x}\text{F}_x]\text{FeAs}$ ($x = 0.05\text{--}0.12$) with $T_c = 26$ K. *Journal of the American Chemical Society* **130**, 3296–3297 (2008).
 - ² Stewart, G. R. Superconductivity in iron compounds. *Rev. Mod. Phys.* **83**, 1589–1652 (2011).
 - ³ Si, Q., Yu, R. & Abrahams, E. High-temperature superconductivity in iron pnictides and chalcogenides. *Nature Reviews Materials* **1**, 16017 (2016).
 - ⁴ Guo, J. *et al.* Superconductivity in the iron selenide $\text{K}_x\text{Fe}_2\text{Se}_2$ ($0 \leq x \leq 1.0$). *Phys. Rev. B* **82**, 180520 (2010).
 - ⁵ Wang, Q.-Y. *et al.* Interface-Induced High-Temperature Superconductivity in Single Unit-Cell FeSe Films on SrTiO_3 . *Chinese Physics Letters* **29**, 037402 (2012).
 - ⁶ Lee, J. J. *et al.* Interfacial mode coupling as the origin of the enhancement of T_c in FeSe films on SrTiO_3 . *Nature* **515**, 245–248 (2014).
 - ⁷ Hsu, F.-C. *et al.* Superconductivity in the PbO-type structure $\alpha\text{-FeSe}$. *Proceedings of the National Academy of Sciences* **105**, 14262–14264 (2008).
 - ⁸ Fang, M. H. *et al.* Superconductivity close to magnetic instability in $\text{Fe}(\text{Se}_{1-x}\text{Te}_x)_{0.82}$. *Phys. Rev. B* **78**, 224503 (2008).
 - ⁹ McQueen, T. M. *et al.* Tetragonal-to-Orthorhombic Structural Phase Transition at 90 K in the Superconductor $\text{Fe}_{1.01}\text{Se}$. *Phys. Rev. Lett.* **103**, 057002 (2009).
 - ¹⁰ Medvedev, S. *et al.* Electronic and magnetic phase diagram of $\beta\text{-Fe}_{1.01}\text{Se}$ with superconductivity at 36.7 K under pressure. *Nat Mater* **8**, 630–633 (2009).
 - ¹¹ Böhmer, A. E. *et al.* Origin of the Tetragonal-to-Orthorhombic Phase Transition in FeSe: A Combined Thermodynamic and NMR Study of Nematicity. *Phys. Rev. Lett.* **114**, 027001 (2015).
 - ¹² Baek, S.-H. *et al.* Orbital-driven nematicity in FeSe. *Nat Mater* **14**, 210–214 (2015).
 - ¹³ Nakayama, K. *et al.* Reconstruction of Band Structure Induced by Electronic Nematicity in an FeSe Superconductor. *Phys. Rev. Lett.* **113**, 237001 (2014).
 - ¹⁴ Shimojima, T. *et al.* Lifting of xz / yz orbital degeneracy at the structural transition in detwinned FeSe. *Phys. Rev. B* **90**, 121111 (2014).
 - ¹⁵ Watson, M. D. *et al.* Emergence of the nematic electronic state in FeSe. *Phys. Rev. B* **91**, 155106 (2015).
 - ¹⁶ Terashima, T. *et al.* Pressure-Induced Antiferromagnetic Transition and Phase Diagram in FeSe. *Journal*

- of the Physical Society of Japan **84**, 063701 (2015).
- ¹⁷ Dai, P. Antiferromagnetic order and spin dynamics in iron-based superconductors. *Rev. Mod. Phys.* **87**, 855–896 (2015).
 - ¹⁸ Yu, R. & Si, Q. Antiferroquadrupolar and Ising-Nematic Orders of a Frustrated Bilinear-Biquadratic Heisenberg Model and Implications for the Magnetism of FeSe. *Phys. Rev. Lett.* **115**, 116401 (2015).
 - ¹⁹ Wang, F., Kivelson, S. A. & Lee, D.-H. Nematicity and quantum paramagnetism in FeSe. *Nat Phys* **11**, 959–963 (2015).
 - ²⁰ Glasbrenner, J. K. *et al.* Effect of magnetic frustration on nematicity and superconductivity in iron chalcogenides. *Nat Phys* **11**, 953–958 (2015).
 - ²¹ Rahn, M. C., Ewings, R. A., Sedlmaier, S. J., Clarke, S. J. & Boothroyd, A. T. Strong $(\pi, 0)$ spin fluctuations in β -FeSe observed by neutron spectroscopy. *Phys. Rev. B* **91**, 180501 (2015).
 - ²² Wang, Q. *et al.* Strong interplay between stripe spin fluctuations, nematicity and superconductivity in FeSe. *Nat Mater* **15**, 159–163 (2016).
 - ²³ Wang, F., Kivelson, S. A. & Lee, D.-H. Nematicity and quantum paramagnetism in FeSe. *Nat. Phys.* **11**, 959 (2015).
 - ²⁴ Shamoto, S. *et al.* Spin nematic susceptibility studied by inelastic neutron scattering in FeSe. *unpublished* (2015). ArXiv:1511.04267.
 - ²⁵ Mukherjee, S., Kreisel, A., Hirschfeld, P. J. & Andersen, B. M. Model of electronic structure and superconductivity in orbitally ordered fese. *Phys. Rev. Lett.* **115**, 026402 (2015).
 - ²⁶ Wang, P. *et al.* Unlocked Stripe-order Antiferromagnetism in FeSe under Pressure. *ArXiv e-prints* (2016). 1603.04589.
 - ²⁷ Kothapalli, K. *et al.* Strong cooperative coupling of pressure-induced magnetic order and nematicity in FeSe. *ArXiv e-prints* (2016). 1603.04135.
 - ²⁸ Yu, R. *et al.* Spin dynamics of a J_1 - J_2 - K model for the paramagnetic phase of iron pnictides. *Phys. Rev. B* **86**, 085148 (2012).
 - ²⁹ Wysocki, A. L., Belashchenko, K. D. & Antropov, V. P. Consistent model of magnetism in ferropnictides. *Nat Phys* **7**, 485 (2011).
 - ³⁰ Wang, Z., Hu, W.-J. & Nevidomskyy, A. H. Spin Ferroquadrupolar Order in the Nematic Phase of FeSe. *ArXiv e-prints* (2016). 1603.01596.
 - ³¹ Lai, H.-H., Hu, W.-J., Yu, R. & Si, Q. Antiferroquadrupolar order and rotational symmetry breaking in a generalized bilinear-biquadratic model on a square lattice. *ArXiv e-prints* (2016). 1603.03027.

- ³² Bauer, B. *et al.* Three-sublattice order in the SU(3) Heisenberg model on the square and triangular lattice. *Phys. Rev. B* **85**, 125116 (2012).
- ³³ White, S. R. Density matrix formulation for quantum renormalization groups. *Phys. Rev. Lett.* **69**, 2863–2866 (1992).
- ³⁴ Gong, S.-S., Zhu, W., Sheng, D. N., Motrunich, O. I. & Fisher, M. P. A. Plaquette Ordered Phase and Quantum Phase Diagram in the Spin- $\frac{1}{2}$ J_1 - J_2 Square Heisenberg Model. *Phys. Rev. Lett.* **113**, 027201 (2014).
- ³⁵ Bendele, M. *et al.* Coexistence of superconductivity and magnetism in FeSe_{1-x} under pressure. *Phys. Rev. B* **85**, 064517 (2012).
- ³⁶ Miyoshi, K. *et al.* Enhanced Superconductivity on the Tetragonal Lattice in FeSe under Hydrostatic Pressure. *Journal of the Physical Society of Japan* **83**, 013702 (2014).
- ³⁷ Kaluarachchi, U. S. *et al.* Nonmonotonic pressure evolution of the upper critical field in superconducting FeSe. *Phys. Rev. B* **93**, 064503 (2016).
- ³⁸ Sun, J. P. *et al.* Dome-shaped magnetic order competing with high-temperature superconductivity at high pressures in FeSe. *ArXiv e-prints* (2015). 1512.06951.
- ³⁹ Terashima, T. *et al.* Fermi surface reconstruction in FeSe under high pressure. *Phys. Rev. B* **93**, 094505 (2016).

Acknowledgments

We thank W. Yu, A. Goldman, A. Böhrer, A. Coldea, and E.M. Nica for useful discussions. The work was supported in part by the NSF Grant No. DMR-1309531 and the Robert A. Welch Foundation Grant No. C-1411 (W.-J.H., H.-H.L. and Q.S.), the NSF Grant No. DMR-1350237 (W.-J.H., H.-H.L. and A.H.N.), a Smalley Postdoctoral Fellowship of the Rice Center for Quantum Materials (H.-H. L.), the National High Magnetic Field Laboratory through the NSF Grant No. DMR-1157490 and the State of Florida (S.-S.G.), the National Science Foundation of China Grant number 11374361 and the Fundamental Research Funds for the Central Universities and the Research Funds of Renmin University of China (R.Y.), and the Robert A. Welch Foundation Grant No. C-1818 (A.H.N.). The majority of the computational calculations have been performed on the Shared University Grid at Rice funded by NSF under Grant EIA-0216467, a partnership between Rice University, Sun Microsystems, and Sigma Solutions, Inc., the Big-Data Private-Cloud Research Cyberinfrastructure MRI-award funded by NSF under Grant No. CNS-1338099 and by

Rice University, the Extreme Science and Engineering Discovery Environment (XSEDE) by NSF under Grants No. TG-DMR160003 and TG-DMR160057. Computational support has also been provided by XSEDE from the NSF under Grant No. DMR-160004 (S.S.G.).

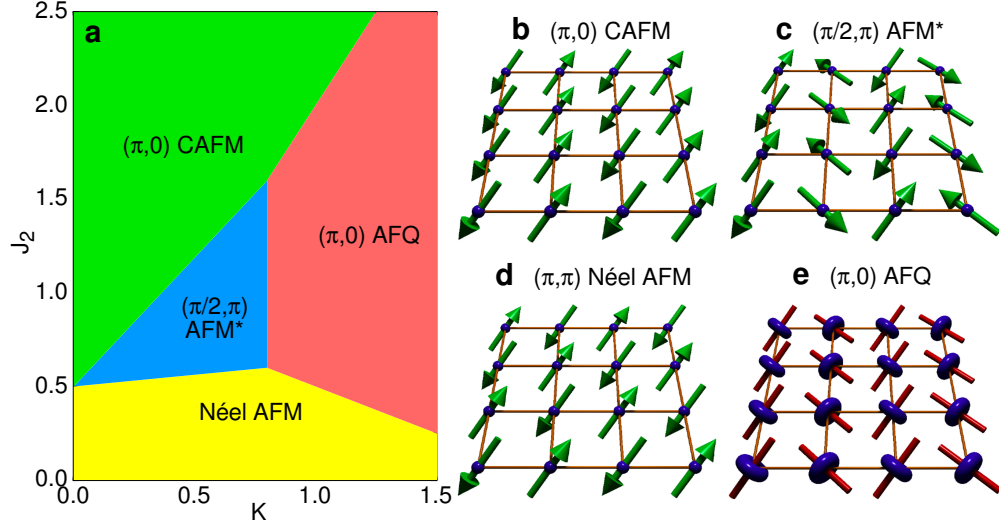


FIG. 1. **Phase diagram and schematic representations for the phases.** (a) Phase diagram of the J_1 - J_2 - K_1 - K_2 - K_3 model with $K_1 = -K_2 = K_3 = -K$ ($K > 0$) on the J_2 - K plane. (J_1 is set to 1.) The phase boundaries are determined from site-factorized wave function calculations. (b)-(e) are schematic illustrations of the four states in (a). The green arrows represent spins. The red cylinders in (e) represent the quadrupolar directors and the blue donut-shaped regimes represent the spin fluctuations which are perpendicular to the directors.

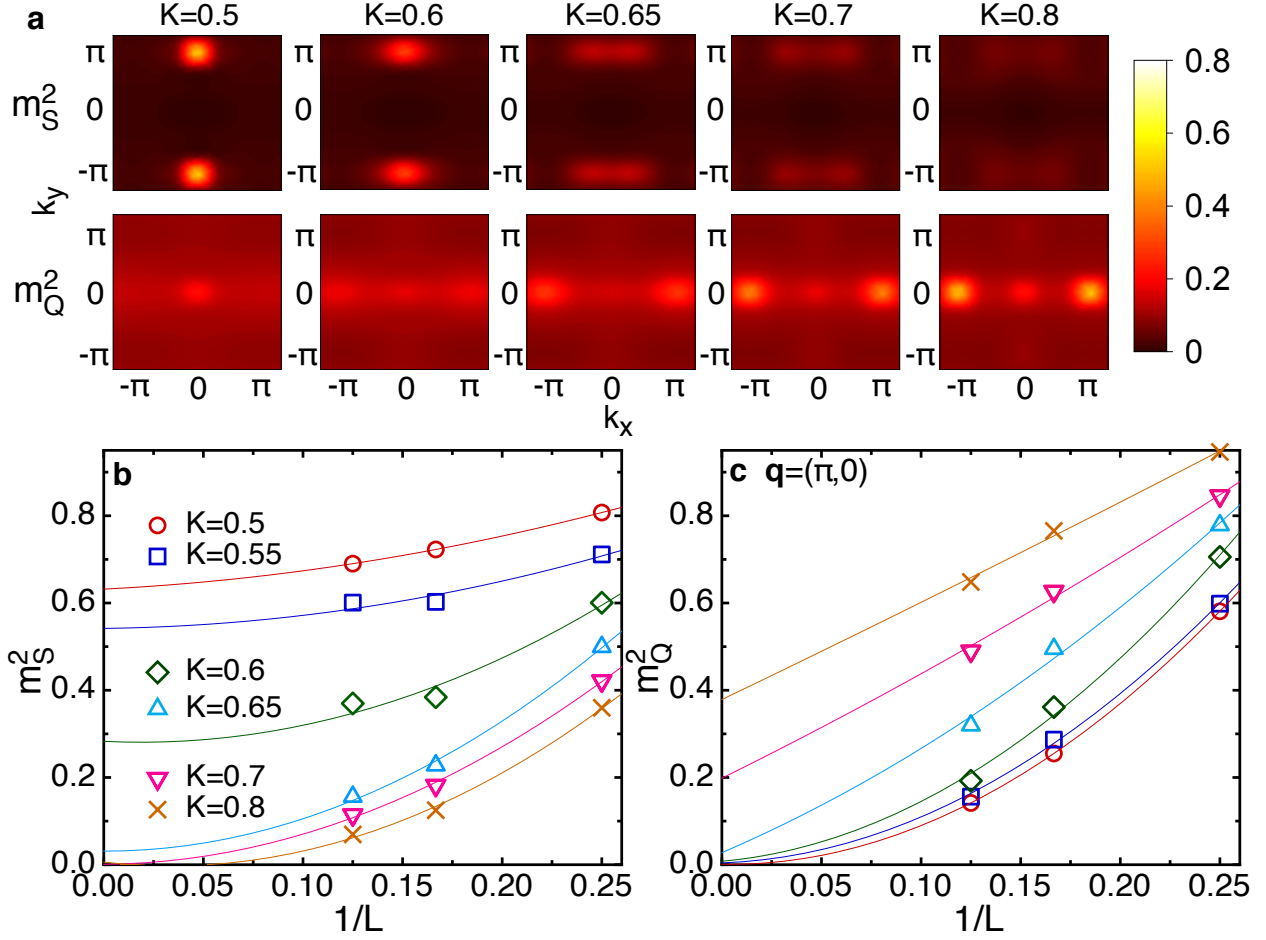


FIG. 2. **Quantum phase transition from CAFM to $(\pi, 0)$ AFQ for $J_2 = 1.5$.** (a) Spin (m_S^2) and quadrupolar (m_Q^2) structure factors obtained from DMRG calculations on the 8×16 cylinder. With growing K , both structure factors simultaneously exhibit dramatic changes at $K \simeq 0.65$, indicating a phase transition from CAFM to $(\pi, 0)$ AFQ. (b) and (c) are the finite-size scaling for the peaks of the spin and quadrupolar structure factors with increasing K , where the lines are guide to the eye. For the quadrupolar structure factors, the momentum $\mathbf{q} = (\pi, 0)$ is chosen. According to the scaling, $K = 0.65$ is close to the phase boundary.

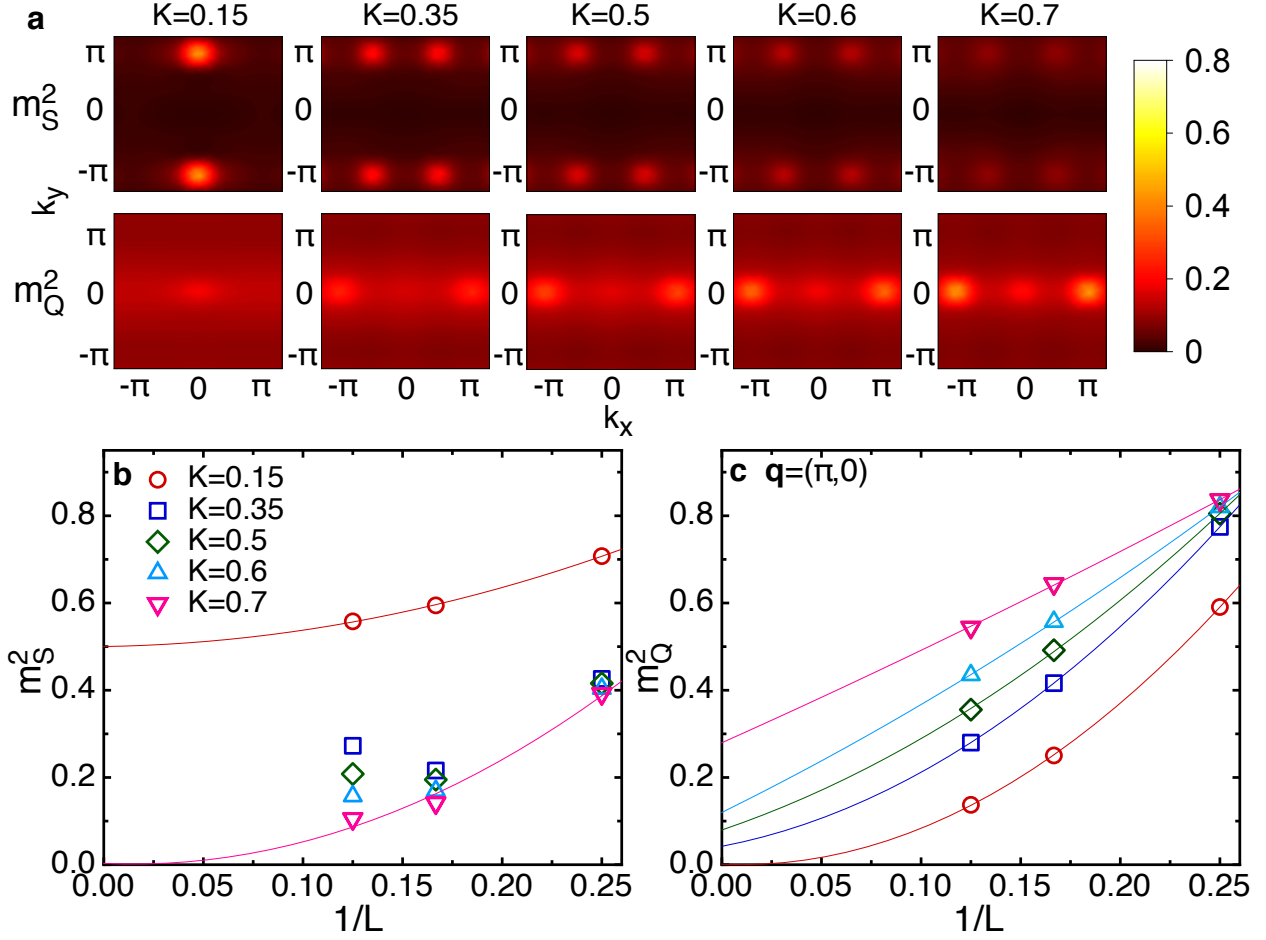


FIG. 3. **Quantum phase transitions of CAFM - $(\pi/2, \pi)$ AFM* - $(\pi, 0)$ AFQ for $J_2 = 0.8$.** (a) Spin (m_S^2) and quadrupolar (m_Q^2) structure factors obtained from DMRG calculations on the 8×16 cylinder. With growing K , m_S^2 shows the first transition from CAFM to $(\pi/2, \pi)$ AFM* at $K \simeq 0.25$ and the next transition to $(\pi, 0)$ AFQ at $K \simeq 0.65$. In both $(\pi/2, \pi)$ AFM* and $(\pi, 0)$ AFQ, m_Q^2 exhibits the characteristic peak at $(\pi, 0)$. (b) and (c) are the finite-size scaling for the peaks of m_S^2 and m_Q^2 with growing K , where the lines are guide to the eye. For the quadrupolar structure factors, the momentum $\mathbf{q} = (\pi, 0)$ is chosen. The momentum $(\pi/2, \pi)$ is not an allowed lattice vector on the 6×6 cluster; this is responsible for the apparent nonmonotonic dependence of m_S^2 vs $1/L$ for $0.25 < K < 0.65$. Results at additional K values are shown in the Supplemental Material.

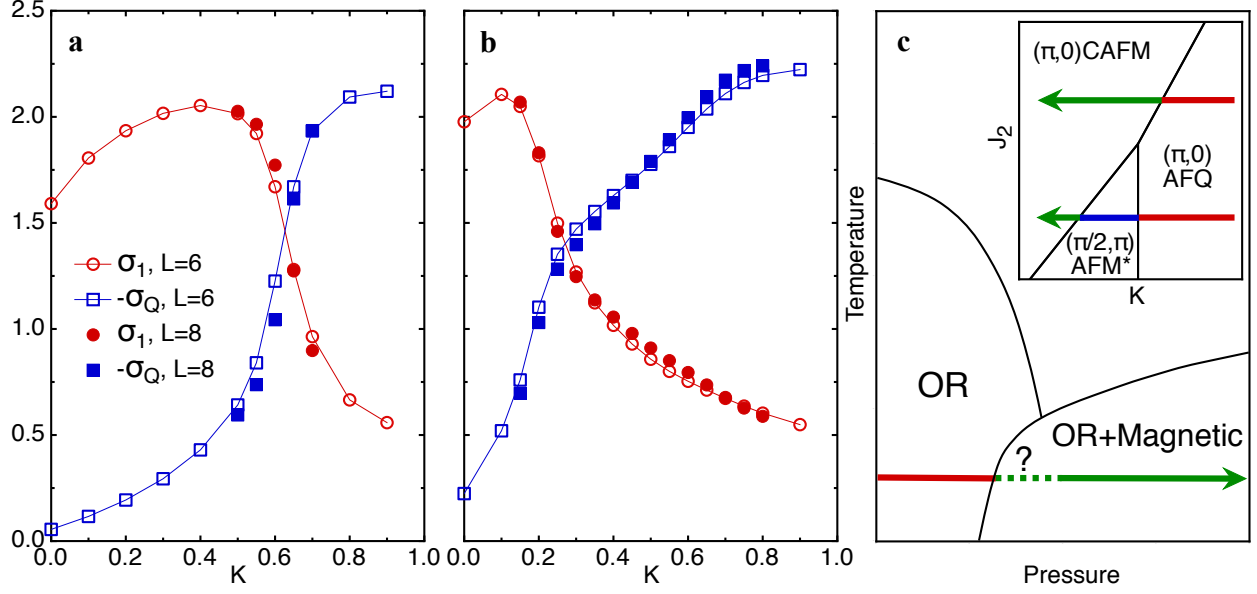


FIG. 4. **Nematicity of the different phases and explanation of the Pressure-Temperature phase diagram of FeSe based on our results.** The spin and quadrupolar nematic order parameters (σ_1 and σ_Q , defined in Eqs.(4) and (5)) as a function of K for (a) $J_2 = 1.5$ and (b) $J_2 = 0.8$ on the $L = 6, 8$ cylinders. (c) The pressure-temperature phase diagram inferred from our theoretical phase diagram (illustrated in the inset, based on Fig. 1(a)). There are two possible sequences of quantum phase transitions from $(\pi, 0)$ AFQ towards CAFM phase, as illustrated by the arrows in both the main panel and the inset.

Supplemental Material

Site-factorized wave-function analysis and phase diagram

For a spin-1 model possibly harboring purely magnetic order, purely quadrupolar order, or coexisting magnetic and quadrupolar orders, it is convenient to choose the time-reversal invariant basis of the $SU(3)$ fundamental representation,

$$|x\rangle = \frac{i|1\rangle - i|\bar{1}\rangle}{\sqrt{2}}, \quad |y\rangle = \frac{|1\rangle + |\bar{1}\rangle}{\sqrt{2}}, \quad |z\rangle = -i|0\rangle, \quad (6)$$

where we abbreviate $|S^z = \pm 1\rangle \equiv |\pm 1\rangle$ ($|S^z = 0\rangle \equiv |0\rangle$) and $|\bar{1}\rangle \equiv |-1\rangle$. Within this basis, the site-factorized wave-functions at each site i which characterize any possible ordered state with short-ranged correlations can be expressed as

$$|\mathbf{d}_i\rangle = d_i^x|x\rangle + d_i^y|y\rangle + d_i^z|z\rangle, \quad (7)$$

where d_i^x, d_i^y, d_i^z are complex numbers and can be re-expressed in the vector form with the basis $\{|x\rangle, |y\rangle, |z\rangle\}$ as $\mathbf{d}_i = (d_i^x \ d_i^y \ d_i^z)$. It is convenient to separate the real and imaginary parts of \mathbf{d}_i as $\mathbf{d}_i = \mathbf{u}_i + i\mathbf{v}_i$. The normalization of the wave-function leads to the constraint $\mathbf{d}_i \cdot \bar{\mathbf{d}}_i = 1$, or equivalently, $\mathbf{u}_i^2 + \mathbf{v}_i^2 = 1$, and the overall phase can be fixed by requiring $\mathbf{d}_i^2 = \bar{\mathbf{d}}_i^2$, i.e., $\mathbf{u}_i \cdot \mathbf{v}_i = 0$. In a pure quadrupolar state, \mathbf{d} will take either a real or imaginary value, but not both, and the associated director is parallel to the director vector \mathbf{d} . This is to be contrasted with a magnetic order, for which \mathbf{d} contains both real and imaginary components, thus yielding a dipolar magnetic moment. Within the framework, we can determine the spin operator from $\mathbf{S}_i = 2\mathbf{u}_i \times \mathbf{v}_i$. In terms of the components of the \mathbf{d} , the spin and quadrupole operators can be written as $S^\alpha = -i \sum_{\beta\gamma} \epsilon^{\alpha\beta\gamma} \bar{d}^\beta d^\gamma$, $Q^{x^2-y^2} = -|d^x|^2 + |d^y|^2$, $Q^{3z^2-r^2} = [|d^x|^2 + |d^y|^2 - 2|d^z|^2]/\sqrt{3}$, $Q^{\alpha\beta}|_{\alpha \neq \beta} = -\bar{d}^\alpha d^\beta - \bar{d}^\beta d^\alpha$.

Within the site-factorized wave-function analysis, we can then re-express the model Hamiltonian as

$$H = \sum_{i,\delta_n} \left[J_n |\mathbf{d}_i \cdot \bar{\mathbf{d}}_j|^2 + (K_n - J_n) |\mathbf{d}_i \cdot \mathbf{d}_j|^2 + K_n \right], \quad (8)$$

where we have fixed $J_3 = 0$ and $-K_1 = K_2 = -K_3 = K > 0$. The variational phase diagram is obtained by numerically minimizing the Hamiltonian above. There are five phases found within the site-factorized wave-function analysis, which are collinear antiferromagnetic phase (CAFM), Néel AFM, $(\pi, 0)$ antiferroquadrupolar phase (AFQ), a newly discovered magnetic phase dubbed $(\pi/2, \pi)$ AFM*, and a phase with coexistence of magnetic and quadrupolar orders at different real-space sites dubbed AFMQ.

The CAFM and Néel AFM show the conventional spin patterns with nearest-neighbor spins parallel or anti-parallel to each other. The $(\pi, 0)$ AFQ is characterized by the mutually orthogonal nearest-neighbor directors, i.e., $\mathbf{d}_i \cdot \mathbf{d}_j = 0 = \mathbf{d}_i \cdot \bar{\mathbf{d}}_j$.

For $(\pi/2, \pi)$ AFM*, the spin pattern along the x -axis can take the periodic pattern as $|S^z = 1\rangle$, $|S^x = 1, |S^z = -1\rangle$, and $|S^x = -1\rangle$, while the spin pattern along the \hat{y} -axis still takes the conventional staggered form.

Within the site-factorized wave-function studies, the phase boundaries between each phase can be determined analytically. We find that the site energies for Néel AFM, collinear AFM (CAFM), $(\pi/2, \pi)$ AFM*, AFMQ, and $(\pi, 0)$ AFQ (we ignore the constant terms and set $(J_1, J_3) = (1, 0)$ in the equations along with $-K_1 = K_2 = -K_3 = K > 0$) are

$$\mathcal{E}_{AFM}^{Néel} = 2(K_1 - J_1) + 2J_2 + 2J_3 = -2 + 2J_2 - 2K, \quad (9)$$

$$\mathcal{E}_{CAFM} = K_1 + 2(K_2 - J_2) + 2J_3 = -2J_2 + K, \quad (10)$$

$$\mathcal{E}_{(\pi/2, \pi)AFM^*} = -J_1 + \frac{5}{4}K_1 + \frac{1}{2}K_2 + K_3 = -1 - \frac{7}{4}K, \quad (11)$$

$$\mathcal{E}_{(\pi, 0)AFQ} = K_1 + 2K_3 = -3K, \quad (12)$$

$$\mathcal{E}_{AFMQ} = -\frac{1}{2}J_1 + K_1 + \frac{3}{2}K_3 = -\frac{1}{2} - \frac{5}{2}K. \quad (13)$$

We can then determine the boundaries between each phase based on these energies

- (1) Phase boundary between Néel AFM and $(\pi, 0)$ AFQ: $K + 2J_2 = 2$.
- (2) Phase boundary between Néel AFM and $(\pi/2, \pi)^*$ AFM: $K - 8J_2 = -4$.
- (3) Phase boundary between Néel AFM and AFMQ: $K + 4J_2 = 3$.
- (4) Phase boundary between $(\pi/2, \pi)$ AFM* and AFMQ: $K = \frac{2}{3}$.
- (5) Phase boundary between AFMQ and $(\pi, 0)$ AFQ: $K = 1$.
- (6) Phase boundary between $(\pi/2, \pi)^*$ AFM and CAFM: $11K - 8J_2 = -4$.
- (7) Phase boundary between AFMQ and $(\pi, 0)$ AFQ: $7K - 4J_2 = -1$.
- (8) Phase boundary between CAFM and $(\pi, 0)$ AFQ: $2K - J_2 = 0$.

The AFMQ shows the same period as that of $(\pi/2, \pi)$ AFM*, but is an inhomogeneous phase with finite magnetic orders and quadrupolar orders at different real-space columns (rows). The spin

pattern in AFMQ takes staggered pattern between magnetically-ordered sites, while the quadrupolar pattern is ferroquadrupolar (FQ), i.e., quadrupolar directors are all parallel to each other. The site-factorized wave-functions between the magnetically-ordered sites and the quadrupolar sites are orthogonal to each other. Since this regime with coexisting magnetic and quadrupolar orders at different columns (rows) appears between the $(\pi/2, \pi)$ AFM and $(\pi, 0)$ AFQ, whose period is consistent with both $(\pi/2, \pi)$ AFM and $(\pi, 0)$ AFQ, it is likely that this phase is just a transition regime between the purely magnetic phase and the purely quadrupolar phase. Its existence reflects the first-order nature of the transition between the two phases, and it is expected to be destabilized by quantum fluctuations; this is confirmed by our DMRG calculations. We have therefore ignored it in the phase diagram in Fig. 1(a).

DMRG results

In this part we present more DMRG results. First we show the real space spin and quadrupolar configurations obtained through the calculations of the spin-spin and quadrupolar-quadrupolar correlation functions by DMRG on $L = 8$ cylinder in Fig. 5. Due to the cylindrical geometry, the CAFM automatically chooses the anti-parallel configuration along the y -direction and the parallel configuration along the x -direction; the AFQ phase has the antiferroquadrupolar configuration along the x -direction and the ferroquadrupolar configuration along the y -direction. In the $(\pi/2, \pi)$ AFM* phase, along the y -direction, the spin configuration is anti-parallel; along the x -direction, the spin pattern in Fig. 5(b) indicates the spins are orthogonal between two nearest neighbor sites. Secondly, we present more data of the spin (m_S^2) and quadrupolar (m_Q^2) order parameters for $J_2 = 0.8$ in Fig. 6, which shows that the first phase transition point is at $K \simeq 0.25$ and the second phase transition is at $K \simeq 0.65$. Finally, we show the finite-size scaling for the nematic order parameters σ_1 and σ_Q of the four phases in Fig. 7. In the Néel AFM, both σ_1 and σ_Q decay fast to vanish with increasing size. For other three phases, the finite-size scaling clearly show the non-zero nematic orders in the thermodynamic limit.

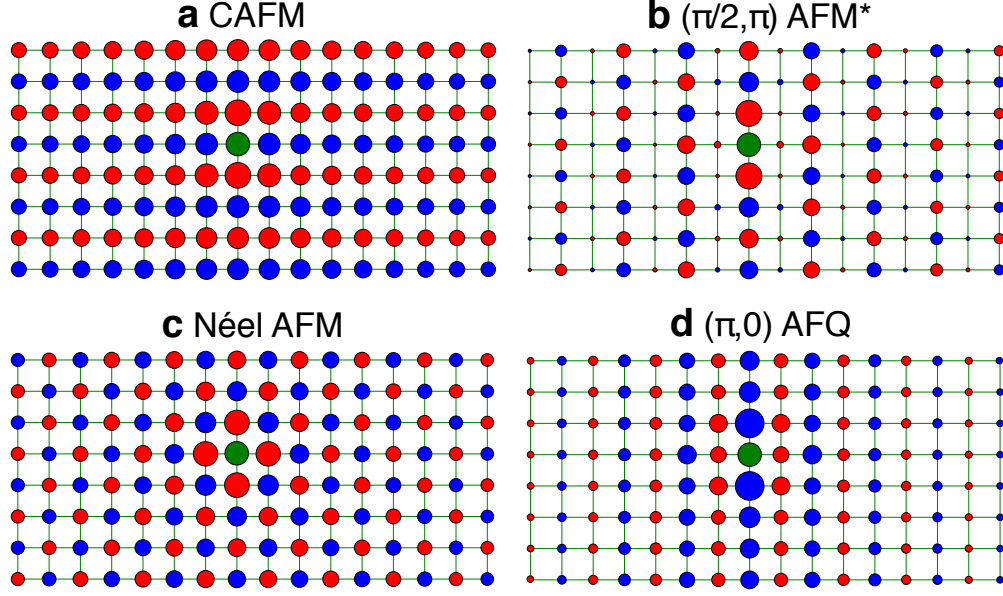


FIG. 5. **Real space spin and quadrupolar correlation functions of the four phases.** (a) The spin correlation for the CAFM at $J_2 = 1.5$ and $K = 0.5$; (b) the spin correlation for the $(\pi/2, \pi)$ AFM* at $J_2 = 0.8$ and $K = 0.35$; (c) the spin correlation for the Néel AFM at $J_2 = 0.4$ and $K = 0.6$; (d) the quadrupolar correlation for the $(\pi, 0)$ AFQ at $J_2 = 1.5$ and $K = 0.7$. The green site is the reference site; the blue and red colors denote positive and negative correlations of the sites with the reference site, respectively. The area of circle is proportional to the magnitude of the spin or quadrupolar correlation.

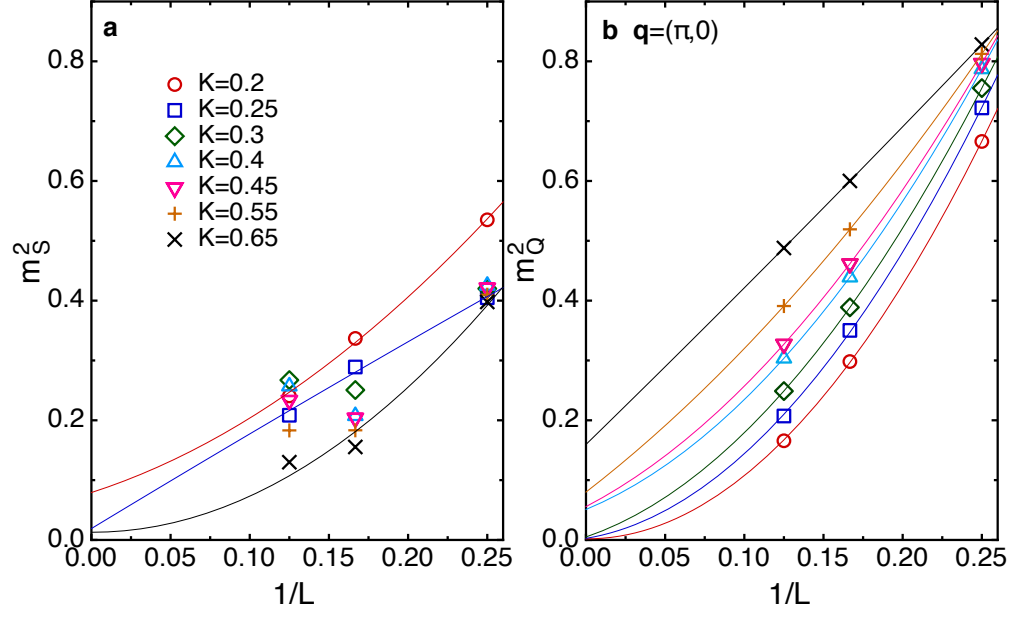


FIG. 6. **Finite-size scaling of spin and quadrupolar order parameters for $J_2 = 0.8$.** To supplement the data in Fig. 3 of the main text, m_S^2 (a) and m_Q^2 (b) are shown with more different K values here. The lines are guided to the eye. For the quadrupolar order in (b), the peak value of the quadrupolar structure factor at the momentum $\mathbf{q} = (\pi, 0)$ is chosen.

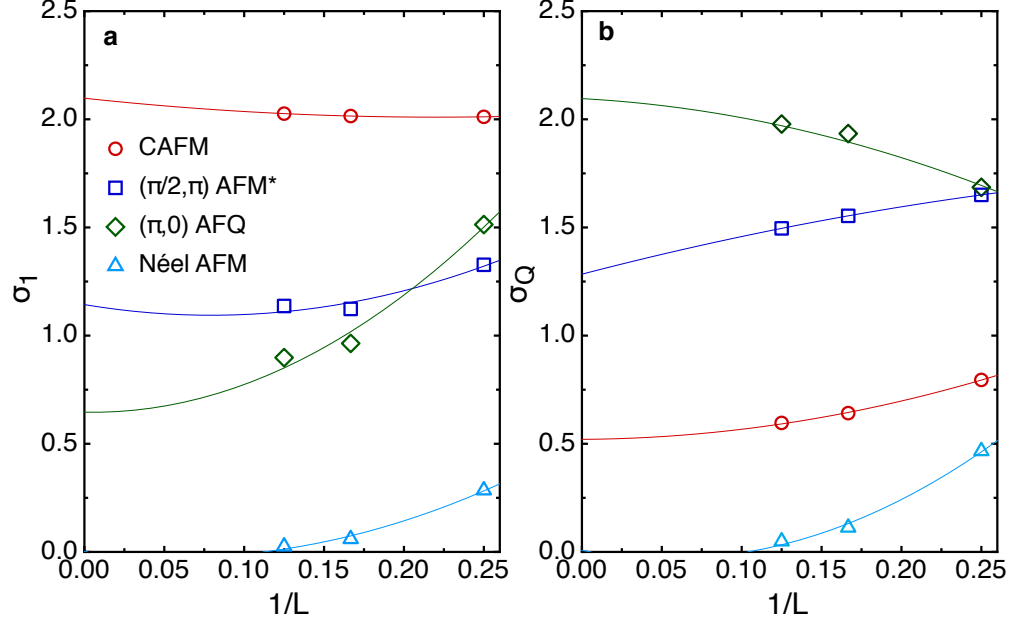


FIG. 7. **Finite-size scaling of nematic order parameters for the four different phases.** The nematic order parameters σ_1 (a) and σ_Q (b) for the CAFM at $J_2 = 1.5, K = 0.5$, the $(\pi/2, \pi)$ AFM* at $J_2 = 0.8, K = 0.35$, the $(\pi, 0)$ AFQ at $J_2 = 1.5, K = 0.7$, and the Néel AFM at $J_2 = 0.4, K = 0.6$.